ACADEMIA
NANO: SCIENCE,
MATERIALS, TECHNOLOGY

Research Article
Published: 3 March 2026
https://doi.org/10.20935/AcadNano8182

Substrate-dependent hardness and adhesion of nano-grained aluminosilicate films by dry aerosol deposition

Arezou Karimian[1], Paul Fuierer[1,*]

Academic Editor: Sergio Javier Mejía Rosales

Abstract

This study explores the fabrication of nanoscale, fine-grained aluminosilicate thick films using dry aerosol deposition (DAD) and investigates how substrate hardness influences film evolution, morphology, and mechanical performance. Amorphous aluminosilicate powders were deposited at room temperature onto aluminum, stainless steel, and glass substrates, representing a wide hardness spectrum (1.5–6 GPa). Scanning electron microscopy (SEM), Atomic force microscopy (AFM), and nanoindentation analyses revealed that substrate hardness plays a role in particle anchoring, initial morphology, and roughness, and final film roughness and hardness. The deposited coatings achieved thicknesses of 5–11 μm with good adhesion. Tensile pull-off strength ranged from 18.5 to 25.3 MPa with predominantly cohesive failure, indicating strong interfacial adhesive bonding. Biaxial loading (scratch testing) of coatings on aluminum revealed average cohesive and adhesive failure loads of 4.4 and 9.0 N respectively. Films deposited on steel exhibited the highest hardness (5.9 GPa), highest tensile pull strength (25 MPa), and no evidence of adhesive failure even at the highest scratch load (25 N), suggesting an optimal energy transfer to particle fracture and particle embedding. These findings highlight the substrate's role in the mechanical properties of DAD coatings, and demonstrate the viability of aluminosilicate as a low-cost, unrefined feedstock for protective DAD coatings.

Keywords: *dry aerosol deposition, aluminosilicate coating, nanoindentation hardness, pull-off adhesion*

Citation: Karimian A, Fuierer P. Substrate-dependent hardness and adhesion of nano-grained aluminosilicate films by dry aerosol deposition. *Academia Nano: Science, Materials, Technology* 2026;3. https://doi.org/10.20935/AcadNano8182

1. Introduction

The marrying of emerging additive modalities with unrefined, natural, and/or waste feedstocks represents an interesting new paradigm in materials engineering and manufacturing. The aerosol deposition (AD) method is a novel, additive, kinetic spray process in which micro-scale ceramic particles are aerosolized and accelerated to sonic speeds using a pressure differential between source and deposition chambers, a carrier gas, and a converging–diverging nozzle. Upon high-velocity impact with the substrate, the brittle particles fracture to nano-scale, releasing localized thermal and mechanical energy that enables bonding to the substrate and adjacent particles [1–4]. As deposition continues, subsequent particles densify the growing film through a hammering effect, forming a mechanically robust ceramic coating without the need for high-temperature sintering [5–7]. Dry aerosol deposition (DAD) is a useful, descriptive name because the process does not rely on any binders or liquid vehicle in forming or depositing [4, 8]. The uniqueness comes with the ability to produce thick films at a high rate and high density at room temperature without any post-heat treatment (i.e., sintering). This means that the nano-scale microstructure is retained, and joining and intermixing of materials while avoiding thermally driven reactions is possible. Myriad applications are envisioned, including functional ceramics like insulating dielectrics for electronics, ion and mixed conductors for batteries and fuel cells, wide-band gap semiconductors for solar cells, and refractory and inert ceramics for protective coatings [9], including for space [10].

Alumina (Al_2O_3) is a well-known, refractory ceramic for which successful film formation has been demonstrated via DAD for over a decade [11, 12]. On the other hand, aluminosilicate (AS) is a relatively unexplored material in aerosol deposition despite its attractive attributes of low density, high hardness, and excellent thermal stability. As an interesting extreme example, high temperature (1300 °C)–high pressure (15.6 GPa) densification of Al_2SiO_5 led to dissociation into an Al_2O_3-SiO_2 nanocomposite with a density of 4.05 g/cm^3 and hardness of 19.3 GPa [13]. Only one paper exists describing the aerosol deposition of an AS, in this case crystalline mullite, $Al_6Si_2O_{13}$, with success resulting in a single phase and dense coatings on silicon substrate [14]. In the interest of potential use as an environmental barrier coating (EBC), exposure to 1573 °K, however, caused grain growth and formation of an Al_2O_3 surface phase and a SiO2 interface phase due to diffusion. Applications involving erosion, wear, and corrosion surface protection at low to moderate temperatures may be more suitable for DAD coatings. Thus, aerosol deposition studies focused on mechanical properties and studies using natural AS powders as feedstock are of interest.

AD development faces challenges, including material-specific processing and deposition efficiency. Feedstock particle size plays a critical role in determining deposition behavior in aerosol

[1]Department of Materials and Metallurgical Engineering, New Mexico Institute of Mining and Technology, Socorro, NM, USA.
*email: paul.fuierer@nmt.edu

deposition processes. Recent micro-cold spray studies [3], which share similar impact consolidation physics with AD, show that ultrafine particles smaller than ~100 nm undergo strong deceleration in the bow-shock region and typically rebound without forming a bonded layer. In contrast, particles within the submicron-to-few-micron range are generally suitable for effective impact consolidation, providing sufficient momentum for fracture and compaction yet avoiding the excessive surface erosion associated with substantially larger particles [15, 16].

While the room temperature process opens possibilities for many substrate types, the efficiency and quality of AD coatings are significantly influenced by substrate mechanical properties. It has been demonstrated that ductile substrates tend to enhance particle anchoring, whereas harder substrates demand higher kinetic energies to achieve effective fracture and chemical bonding [9, 17]. Computational models support this by indicating that substrate hardness governs the shift between adhesion-dominated and cohesion-dominated growth regimes [3, 9].

Further understanding is needed on how substrate hardness and surface conditions affect film microstructure and adhesion. Furthermore, virtually all AD research is conducted using refined, often chemically prepared ceramic powders. Due to low deposition efficiency, there is a need to search for cost-effective feedstock that can yield useful ceramic and/or composite coatings. In this study, we investigate, for the first time, the use of natural aluminosilicate (AS), a waste powder from industrial grinding operations, as a feedstock for DAD to form mechanically robust ceramic coatings. The brittle nature of the particles allows their fragmentation upon impact, which is essential for successful consolidation in the DAD process. The influence of substrate mechanical properties (i.e., hardness) on the resulting coating morphology, thickness, and cohesive/adhesive strength is evaluated and related to differences in the initial interfacial anchor layer. This investigation not only explores a novel feedstock for protective ceramic coatings, but also contributes to a deeper understanding of the particle–substrate interactions that govern film formation in DAD.

2. Materials and methods

2.1. Powder feedstock

The feedstocks used for DAD are the waste "fines" from the commercial grinding operation of igneous, feldspathic mineral. The reported nominal chemical composition is 81.17% SiO_2, 7.96% Al_2O_3, 6.92% Na_2O, 4.65% K_2O, 3.17% CaO. The true density of the particles was measured using a gas pycnometer (Anton Paar- Ultrapyc 5000) and was found to be 2.582 g/cm^3. X-ray diffraction (XRD) analysis reveals a significant glassy phase, with the main crystalline phase identified as sodium feldspar (albite).

Figure 1 presents the SEM micrograph of the as-received powder. The particles show irregular morphology, dominated by somewhat equiaxed smaller particles, and angular larger particles with sharp edges and flat surfaces. This morphology reflects the fractured, glassy nature of the material. The surface texture of the particles themselves is relatively smooth at the submicron scale, with no visible porous or sponge-like features. The combination of morphology and brittle nature was expected to facilitate efficient aerosolization, fragmentation upon impact, and strong mechanical interlocking during deposition by the DAD method. Particle size analysis via the line intercept method using field emission scanning electron (FE-SEM, JSM-IT700HR, JEOL) micrographs indicated that the as-received powder has a mean diameter of 3 μm.

2.2. Substrate

Three different substrate materials were used to investigate the aerosol deposition behavior of the aluminosilicate feedstock: microscope glass slides (Am Scope, BS-72P-100S-22), 304 stainless steel, and 6061-grade aluminum (99.9% purity). Substrates were cut or snapped into approximately 20 mm × 20 mm square coupons, with as-received thickness of approximately 1 mm. The materials were selected to represent a range of hardness, glass (~6 GPa), steel (~3 GPa), and aluminum (~1.5 GPa) in order to study how substrate hardness influences coating formation and adhesion.

Surface roughness and morphology are critical factors influencing anchor layer formation. A controlled roughness around 100 nm increases the available surface area and enhances mechanical interlocking between the coating particles and metallic substrates, which is essential for effective adhesion [18]. Stainless steel substrates, with a native roughness near 100 nm, were used as received. Aluminum substrates were mechanically polished using 600, 800, and 1200 grit SiC abrasive papers, reducing their surface roughness to approximately 100 nm. Glass substrates were left unmodified due to their naturally smooth and low roughness surfaces. Before deposition, all substrates were cleaned with isopropanol using optical wipes to eliminate surface contaminants, and polyimide tape was applied along the edges as a mask to define sharp film boundaries.

2.3. Deposition

All films were deposited using the custom DAD system at New Mexico Tech, as shown in **Figure 2**. Just prior to deposition, the feedstock powder was heated in a drying oven at 250 °C for 2.5 h to eliminate adsorbed moisture, and then immediately loaded into the aerosol source chamber. At system startup, a fluidized bed was created using a mechanical vibrating system, with nitrogen gas flow from underneath to promote aerosolization. The aerosol was directed through plumbing to the nozzle positioned inside the vacuum chamber and beneath the substrate, with its exit orifice 5 mm from the substrate surface. The nozzle was De Laval, converging–diverging type, with outlet slit size 10 × 0.5 mm. The gas flow rate and vibration frequency were controlled to maintain a relatively constant powder aerosolization rate and particle flux. Following preliminary optimization experiments, the nominal deposition parameters used included: feedstock powder mass = 20 g, vibration power = 52%, gas flow = 8 L/min, scan speed = 100 mm/min. A high particle impact speed enabled effective fracture and densification of particles, resulting in strongly adherent films [19]. After depositing, the coated sample was annealed at 150 °C for 12 hr. in air atmosphere to remove residual compressive stress, which is a well-known phenomenon in such film [12, 20].

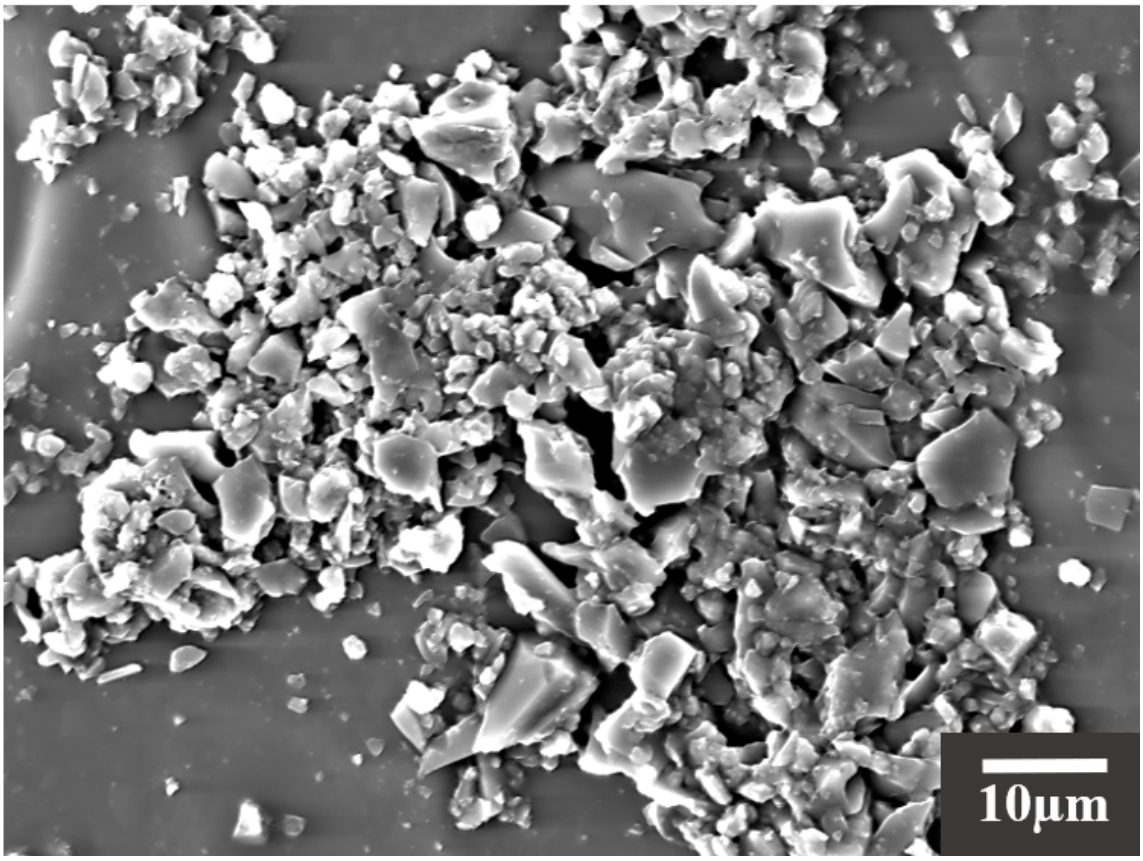


Figure 1 • Scanning electron microscopy (SEM) micrographs of as-received powder.

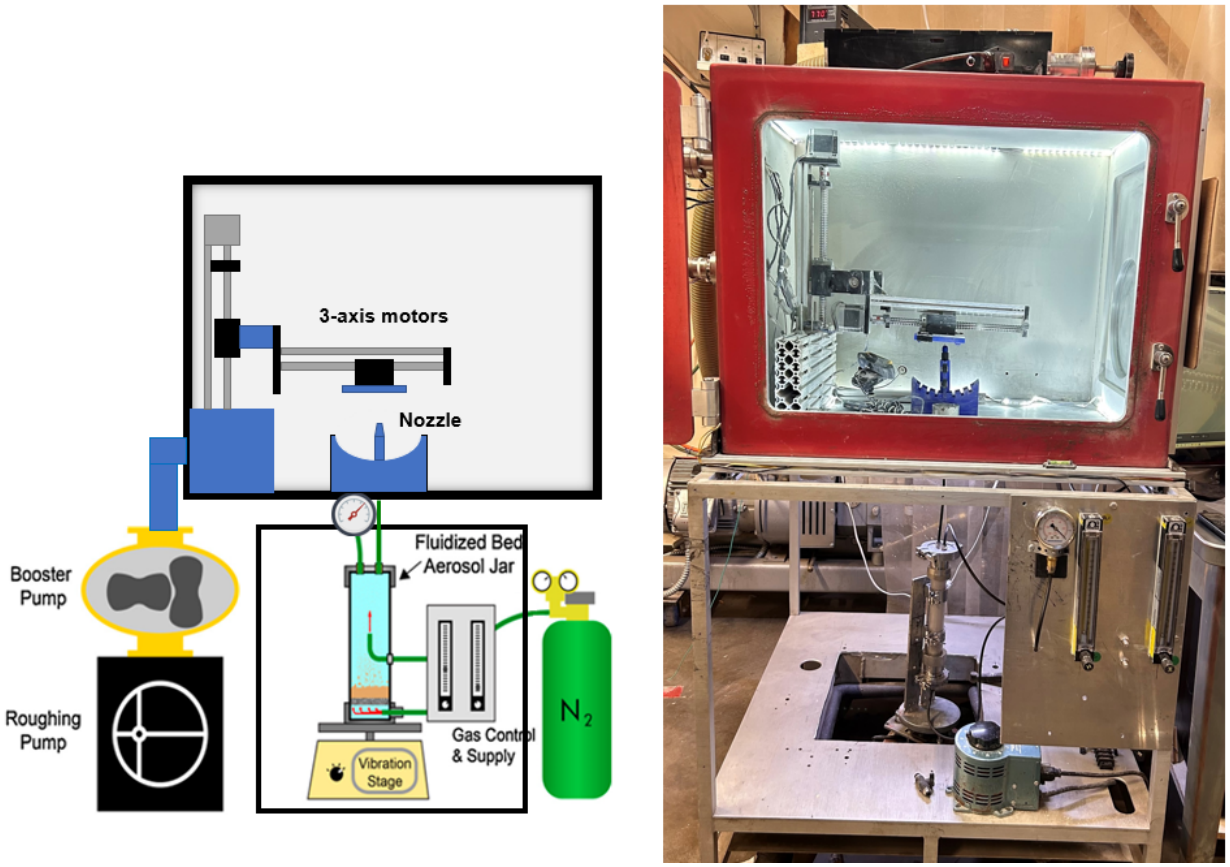


Figure 2 • Schematic (**left**) and photograph (**right**) of the dry aerosol deposition (DAD) system at New Mexico Tech, showing the deposition chamber, 3-axis stage, nozzle, aerosol jar, gas supply and control, and pumping system.

2.4. Characterization

3D surface roughness and film thickness were evaluated using a white-light scanning 3D optical profilometer (ZeGage, Zygo Inc., Middlefield, CT, USA). Film thickness was measured via step-height analysis across the interface between the masked and coated regions of each substrate. Surface morphology and microstructural features of the as-received powder, film surfaces, and cross-sections were observed using a Field Emission Scanning Electron Microscope (FE-SEM; JSM-IT700HR, JEOL, Peabody, MA, USA). Samples were coated with a thin platinum layer to reduce charging during imaging. Imaging was performed at an accelerating voltage of 15 kV and a working distance of 10–14 mm. Atomic force microscopy (Multimode Nanoscope IIIa-Bruker, Santa Barbara, CA, USA) was employed to characterize the surface topography and local (small-area) roughness of the deposited films. For each scan size (5 × 5 μm and 12.5 × 12.5 μm), three independent scans were acquired at different surface locations, and an average roughness, Ra, was calculated.

X-ray diffraction (XRD) analysis was carried out to assess the crystallinity of the coatings. A Bruker D8 Advance diffractometer equipped with Cu Kα radiation (λ = 1.5406 Å) was used. Data were collected over a 2θ range of 10°–70°, with an increment of 0.020°. Phase identification and peak analysis were conducted using Bruker's Evaluation software. Nanoindentation tests were performed (PB1000 Nanoindenter, Nanovea, Grugliasco, Italy) to measure the hardness of both coated and uncoated substrates. To ensure accuracy in nanoindentation tests, the ISO 14577 standard [21] specifies that surface roughness (Ra) should be less than 5% of the maximum indentation depth [22]. Therefore, surface roughness was carefully minimized through extensive polishing using 3.0, 1.0, and 0.3 μm alumina slurries consecutively for total times of 3.5 h (glass), 5 h (steel), and 4.5 h (aluminum). A Berkovich diamond tip was used and indentation was performed with a maximum load of 10 mN, dwell time of 10 s, approach speed of 7 μm/min, loading rate of 10 mN/min, and unloading rate of 20 mN/min. To minimize substrate effects, the penetration depth was kept below 10% of the total film thickness. Hardness (H) and elastic modulus (E) were calculated from the load–displacement curves: H from the maximum point, and E from the slope of the unloading curve. Following ASTM E2546 [23] guidelines for instrumented indentation testing, twenty randomly distributed indents were performed on each surface coating (ten for bare materials) to ensure statistical reliability.

Adhesion strength was quantified by a uniaxial pull testing (ASTM C633/D4541) [24, 25] using a Mark-10 universal testing machine. Aluminum dollies with machined circular flats of diameters of 10 mm were bonded to the coated surfaces with a two-part epoxy adhesive (max strength 35 MPa), cured for 48 h at ambient conditions to ensure reliable bonding. Three specimens were tested for each substrate (steel, glass, and aluminum), and the maximum detachment stress was recorded as the adhesion strength. Scratch testing was performed according to ASTM C1624-05 [26] using a test system equipped with a micro conical 98 indenter (Rockwell "C" diamond, 120° cone with 200 μm radius). The starting load was 0.1 N, gradually increasing to a final load of 25.1 N at a rate of 5 N/min. The lateral speed was 1 mm/min, with 5 min tests producing a scratch length of 5 mm. Three scratch tests were carried out on each of the three coatings on aluminum and steel substrates. According to ASTM C1624 [26] standards, each scratch track was examined under a microscope for evidence of LC1, corresponding to the onset of cracking and loss of cohesion, and LC2, corresponding to the point where a crack or delaminated region bridges across the scratch track, indicating loss of coating adhesion.

3. Results

3.1. DAD film characteristics and microstructures

Films were successfully deposited onto all three substrate materials as shown in **Figure 3**. All films were intact and robust, exhibiting good adhesion, initially confirmed qualitatively by a tape test similar to ASTM D3359 [27] (and further validated by quantitative pull-off adhesion testing described in Section 3.4). Films on glass and steel had 10 μm nominal thickness, whereas those on aluminum had a 6 μm thickness, as measured by an optical profiler (**Figure 4**). Cross-sectional SEM images in **Figure 5** reveal thicknesses in agreement with profilometry measurements. Edge views give the impression that the film on steel is the densest and smoothest; however, it is noted that the different substrates are amenable to different cross-sectional preparation: glass was fractured, steel was cut and lightly ground and cleaned, and aluminum was AD coated up to its edge.

Thus, cross-sectional microstructures are not directly comparable. Nonetheless, all three appear to be free of micro–macro-pores and open porosity, which is expected of aerosol-deposited films. Closed nano-porosity may in fact be present, but not observable at achievable resolution. The surface microstructures consist of fine grains with ill-defined grain boundaries, also typical of AD films. This microstructure arises from the hammering effect [5, 7], where high-velocity particle impacts act to fragment the particles, followed by realignment and compaction via successive collisions. Crater-like surface features can be attributed to large particle impacts [28–30].

Anchor layer formation is a key determinant of the adhesion and durability of AD films [31], and its quality can influence the ultimate thickness achieved during subsequent build-up. The SEM images in **Figure 6** are after the very first pass of the nozzle, and reveal stark differences in the nature of the anchor layer across substrates. The layer on aluminum appears nodular, with rounded nodules about a micron in diameter. The layer is quite thick and contains voids and/or fractures. The anchor layer on steel is very different, with flake-like features and very small particles embedded into the deep crevices between flakes. The flake-like features have the appearance of shear bands, which are narrow, planar zones of highly concentrated plastic strain that form during intense shearing [32].

It looks as though significant shear deformation has taken place in the steel due to the high strain rates from the high-speed particle impacts, which is the bonding mechanism in cold spray. The anchor layer on glass does not exhibit such shear features, but rather there is a coalescence of small particles into larger islands, similar to aluminum, but not as nodular, and without major voids or cracks. **Table 1** compares values for thickness and roughness of both anchor layers and final films on the three substrates. The higher anchor layer thickness and roughness and also presence of major defects on aluminum are believed to be significant.

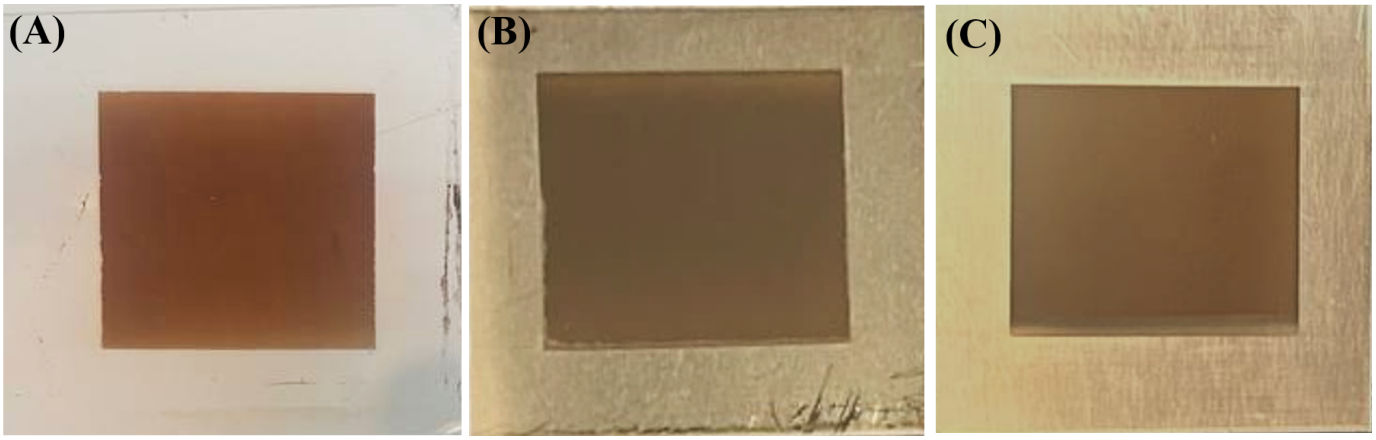


Figure 3 • Optical images of coated substrates of (**A**) glass, (**B**) steel, and (**C**) aluminum, each with nominal coated area of 15 mm × 15 mm.

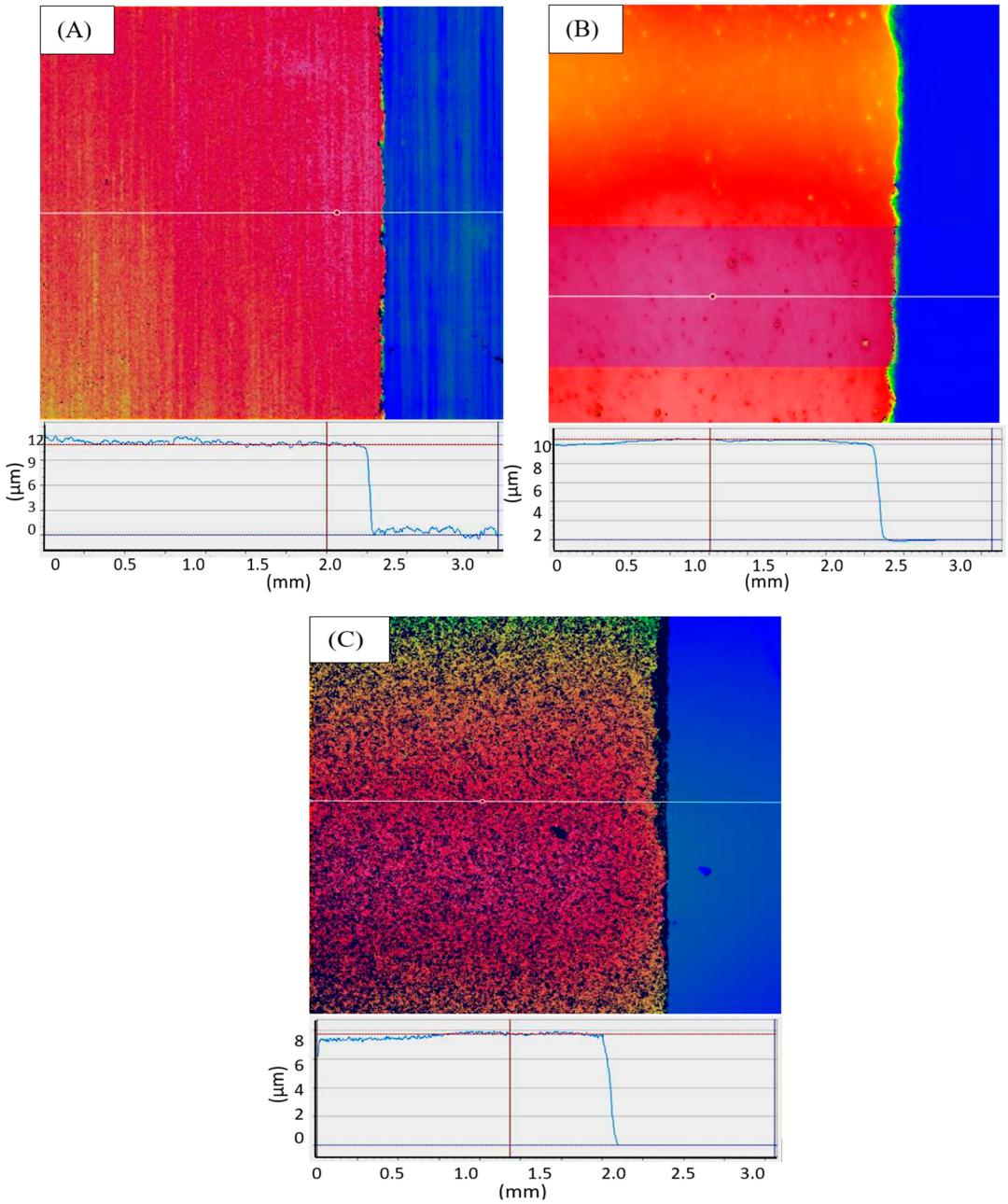


Figure 4 • Optical profiler images of coated substrates of (**A**) glass, (**B**) steel, and (**C**) aluminum, with the stepped-edge revealing film thickness.

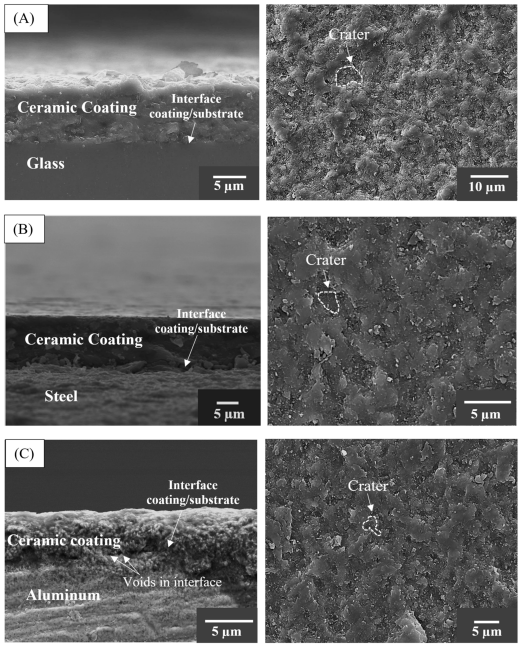


Figure 5 • DAD aluminosilicate ceramic coatings on (**A**) glass, (**B**) steel, and (**C**) aluminum substrates, showing top views (right) and cross-sections (left).

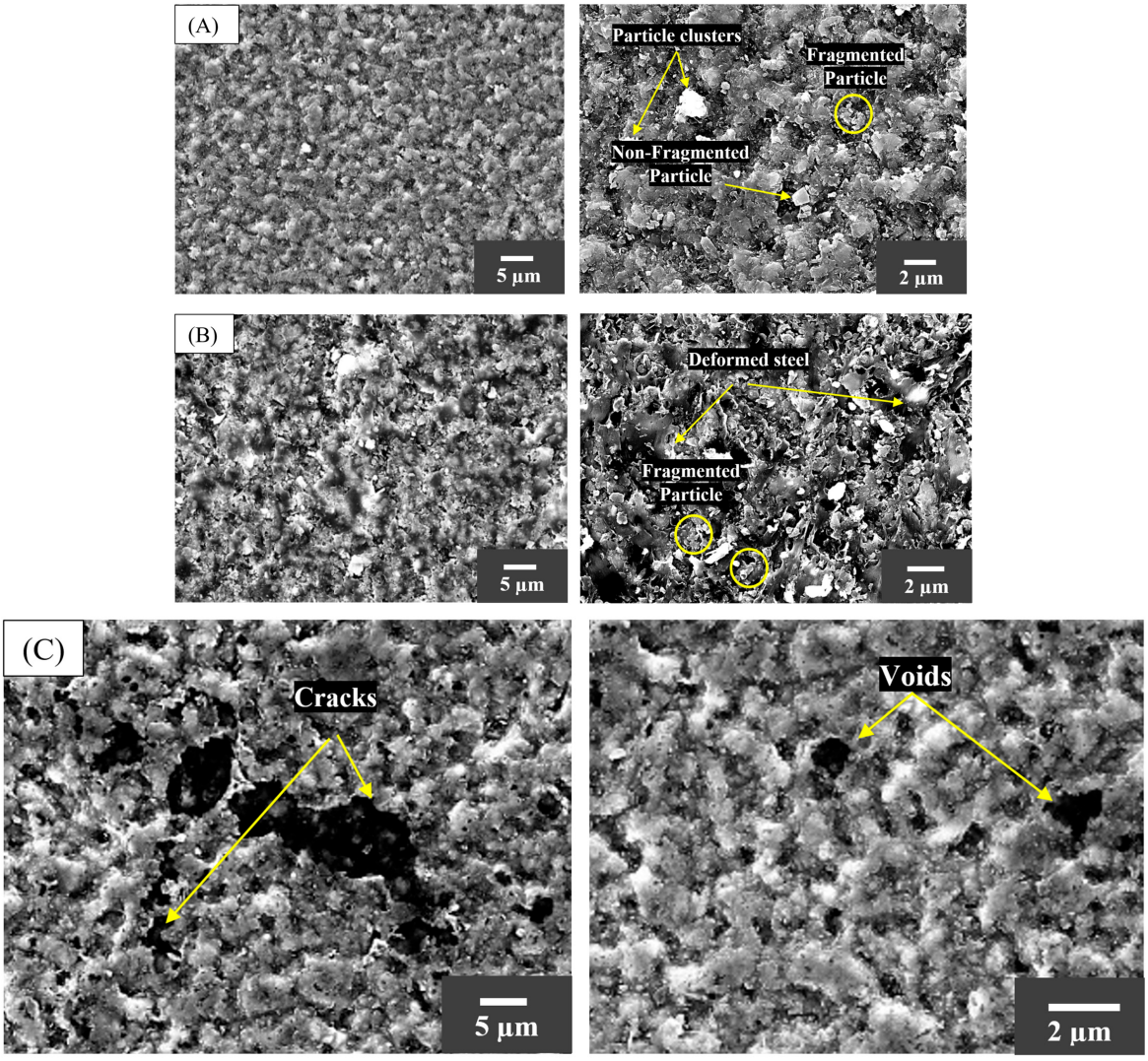


Figure 6 • First (anchor) layer after one scan deposition on (**A**) glass, (**B**) steel, and (**C**) aluminum substrates.

Table 1 • Thickness and roughness of anchor layers and final coatings deposited on glass, steel, and aluminum substrates.

	Glass	Steel	Aluminum
Thickness (anchor-μm)	0.501	0.450	0.710
Roughness (anchor-μm)	0.233	0.324	0.352
Thickness (final-μm)	11.0	10.6	6.0
Roughness (final-μm)	0.820	0.80	1.36

3.2. Crystallinity and phase composition

Figure 7 presents the XRD patterns of both as-received powder and the deposited film on glass substrate. Quantitative phase analysis via Rietveld refinement revealed that the feedstock powder consists of 51.9% crystalline content and 48.1% amorphous. The crystalline component was exclusively identified as albite ($NaAlSi_3O_8$, JCPDS 01-071-1151, triclinic), with refined lattice parameters (a = 8.144(3) Å, b = 12.788(5) Å, c = 7.160(2) Å, α = 94.26°, β = 116.59°, γ = 87.68°) matching geological albite standards. The amorphous fraction was quantified by subtracting the fitted albite peak intensities and normalizing the remaining diffuse scattering (2θ = 15–35°) against the certified amorphous profile commercial fused silica glass.

The deposited film exhibited significantly reduced crystallinity (15.3%), evidenced by: (i) attenuation of albite peak intensities (particularly the ($\bar{2}01$) reflection at 22.1°), and (ii) broadening of the amorphous halo (full width of half maximum (FWHM) increased from 8.5° to 12.3°). This structural change is attributed to amorphization during aerosol deposition, where (i) high-velocity particle impacts (300–600 m/s [33]) induce defect accumulation in albite crystals, (ii) room temperature deposition kinetically suppresses recrystallization, and (iii) localized heating is insufficient for albite nucleation [34].

3.3. Nano-mechanical properties

The mechanical properties of the DAD ceramic surface coatings were evaluated using nanoindentation testing. AFM images in **Figure 8** show the coating topography before and after polishing. The "Before" images for glass and steel substrates are typical for DAD films, showing crystallite sizes of about 80 nm to 300 nm, and an apparently high roughness with cratering as in the surface SEMs. The "nodules" on the aluminum coating appear to be made up of somewhat larger primary crystallites/grains. The polishing process clearly reduced surface roughness.

The final roughness, measured by AFM over a 5 μm × 5 μm area (relevant for the indentation area), was approximately 5–8 nm, which is well below 10% of the maximum indentation depth. This criterion is essential to avoid surface irregularities interfering with the penetration response of the indenter tip. Measured roughness values are given in **Table 2**. The nano-mechanical load–displacement curves are presented in **Figure 9**. **Figure 10** shows a few indents that were able to be found post-test.

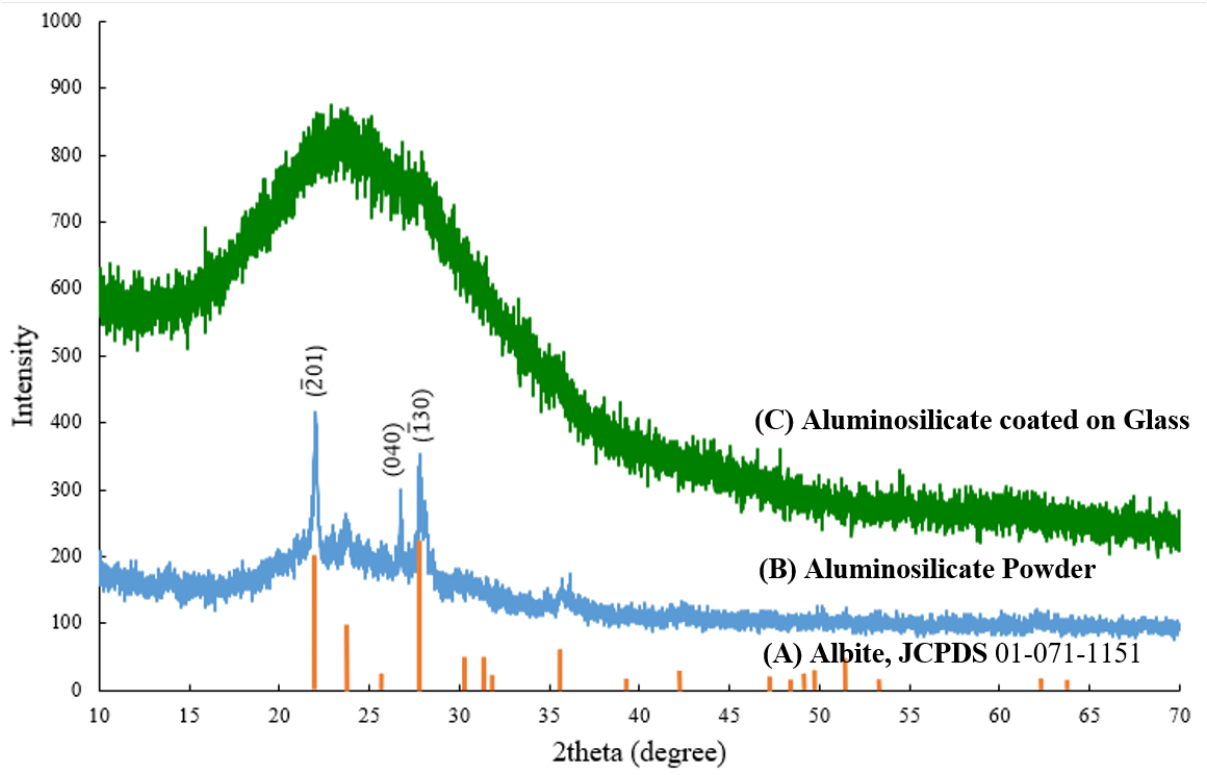


Figure 7 • X-ray diffraction (XRD) patterns of (**A**) sodium aluminum silicate (albite, orange); (**B**) aluminosilicate feedstock powder (blue); (**C**) DAD-aluminosilicate on glass (green).

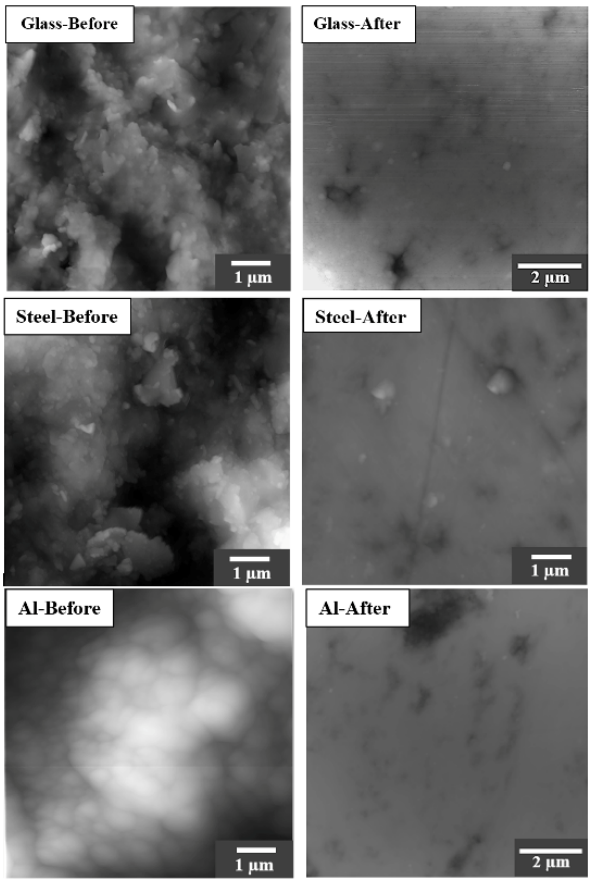


Figure 8 • Atomic force microscopy (AFM) images of DAD ceramic surface coatings before and after polishing for glass, steel, and aluminum substrates.

Table 2 • AFM surface roughness of substrates before, after coating, and after polishing.

Substrate	**$R_{a,subsrate}$ (µm)**	**$R_{a,coating}$ (µm)**	**$R_{a,polish}$ (µm)**
Glass	0.008	0.820	0.005
Steel	0.100	0.797	0.005
Aluminum	0.100	1.335	0.008

The data in **Table 3** reveal that DAD ceramic coatings significantly enhanced surface hardness relative to bare metal substrates increasing aluminum's hardness by 166% (from 1.59 ± 0.23 GPa to 4.24 ± 0.23 GPa) and steel by 89% (from 3.13 ± 0.24 GPa to 5.93 ± 0.92 GPa). The DAD coating on glass was lower than the glass itself (4.95 ± 0.77 GPa vs. 6.14 ± 0.53 GPa). Notably, coatings on stainless steel exhibited the highest hardness (5.93 GPa), suggesting that the substrate's intermediate hardness (3 GPa) optimally balances particle anchoring and energy dissipation during impact, promoting fracture-driven densification.

Statistical analysis via one-way analysis of variance ANOVA (**Table 4**) confirmed significant substrate-dependent differences in coating hardness (p = 0.00192). Post hoc pairwise t-tests showed that steel coating was significantly harder than coating on aluminum (p = 0.01252, Cohen's d = 1.8) and glass (p = 0.00192, d = 1.2), while glass and aluminum coatings were statistically indistinguishable (p = 0.61064, d = 0.3). To address potential non-normality, we additionally verified these trends using Kruskal–Wallis non-parametric tests (H = 14.2, p = 0.0008), which corroborated the ANOVA results without requiring data transformation. The large effect sizes (Cohen's d > 0.8) for significant comparisons underscore the relevance of these findings. Elastic modulus trends (**Table 3** and **Table 5**) diverged from hardness behavior, with coatings on steel (47.62 ± 7.45 GPa) and aluminum (48.53 ± 5.63 GPa) exhibiting 27% higher stiffness than those on glass (38.39 ± 6.58 GPa; ANOVA p = 6.11×10^{-6}).

3.4. Adhesion/cohesion strength

Tensile pull strength test results are shown in **Table 6**, with average values of 25.27 MPa for steel, 24.16 MPa for glass, and 20.85 MPa for aluminum. The trend (steel > glass > aluminum) mirrors the hardness data. Analysis of **Figure 11** indicates that detachment occurred predominantly by cohesive fracture within the coating, rather than adhesive delamination at the film–substrate interface. Substrate surface was generally not observed on failure surfaces, but rather a mix of ceramic coating and epoxy, meaning that either coating or epoxy failed. The maximum strength of the cured epoxy is specified at 35 MPa, and a couple of these tests approached this value.

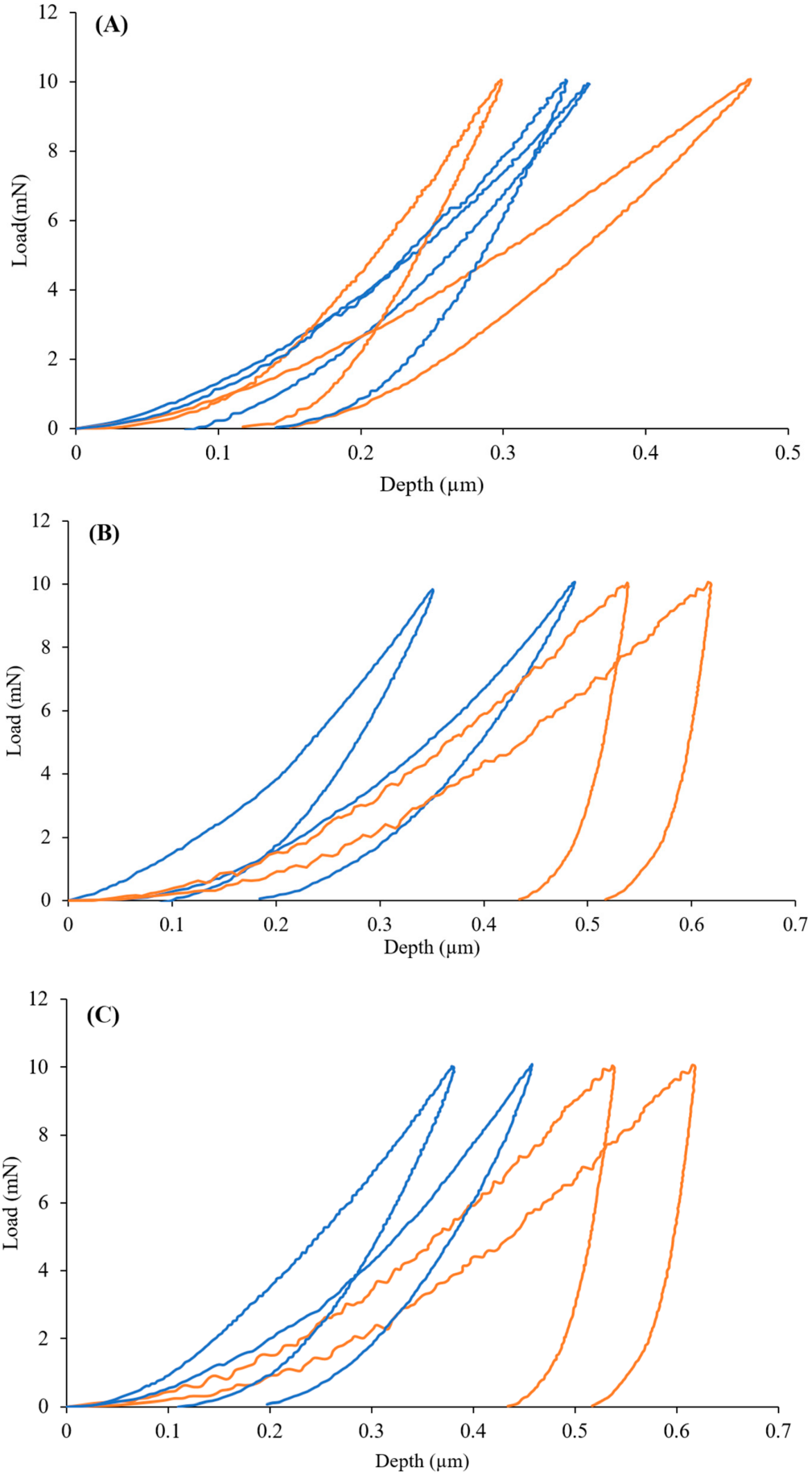


Figure 9 • Representative load–displacement curves for bare (orange) and DAD ceramic coated (blue) substrates: (**A**) glass, (**B**) steel, (**C**) aluminum.

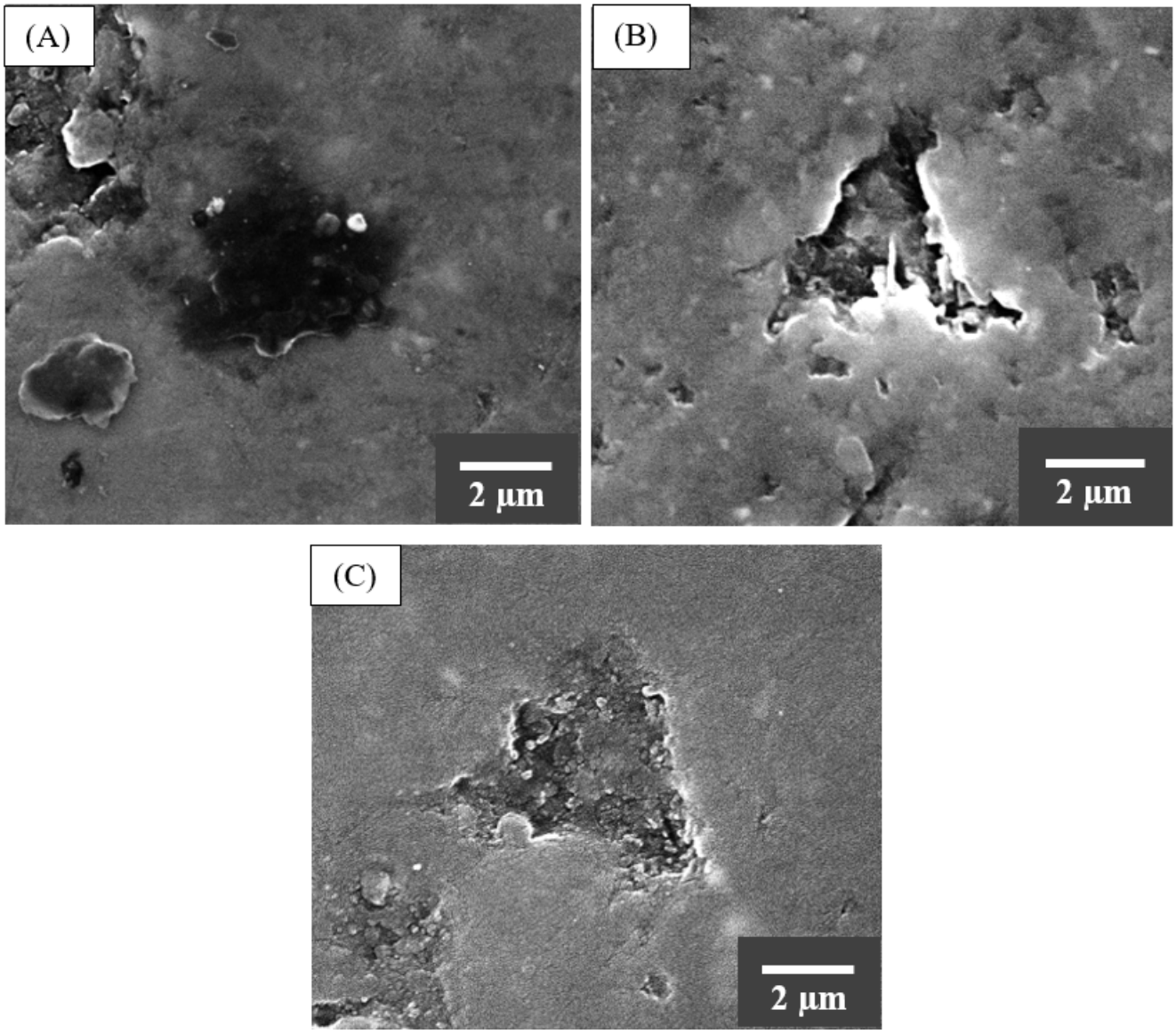


Figure 10 • SEM image of a nanoindentation on the polished surface coating on (**A**) glass, (**B**) steel, and (**C**) aluminum.

Table 3 • Hardness (H) and elastic modulus (E) of bare and coated substrates.

Substrate	**H_{Bare} (GPa)**	**E_{Bare} (GPa)**	**H_{Coated} (GPa)**	**E_{Coated} (GPa)**
Glass	6.14 ± 0.53	64.84 ±3.10	4.95 ± 0.77	38.39 ± 6.58
Steel	3.13 ± 0.24	152.96 ± 12.45	5.93 ± 0.92	47.62 ± 7.45
Aluminum	1.59 ± 0.23	97.51 ± 11.80	4.24 ± 0.23	48.53 ± 5.63

Note: Values are expressed as mean ± standard deviation (SD). Means were calculated from 10 indents for bare substrates and 20 indents for coated substrates.

Table 4 • Statistical comparison (mean difference, *p*-value, significance) of hardness values between coated substrates, including ANOVA results.

Comparison	**Mean difference (GPa)**	***p*-value**	**Significance**
Glass vs. Al	0.74	0.61064	Not significant
Glass vs. Steel	−0.98	0.00192	Significant
Al vs. Steel	−1.72	0.01252	Significant
ANOVA (overall)	–	0.00192	Significant

Table 5 • Statistical comparison (mean difference, *p*-value, significance) of elastic modulus values between coated substrates, including ANOVA results.

Comparison	Mean difference (GPa)	*p*-value	Significance
Glass vs. Al	−10.93	4.20×10^{-6}	significant
Glass vs. Steel	−9.23	0.00093	Significant
Al vs. Steel	1.69	0.26059	Not Significant
ANOVA (overall)	–	6.11×10^{-6}	Significant

Table 6 • Adhesion strength (MPa) of coatings on glass, steel, and aluminum substrates based on three pull tests per coating. Note: All failures occurred via cohesion within the coating.

Test num.	Glass	Steel	Aluminum
Test 1	25.12	32.11	21.47
Test 2	19.29	22.75	18.71
Test 3	28.07	20.96	22.37
Avg	24.16 ± 4.47	25.27 ± 5.99	20.85 ±1.91

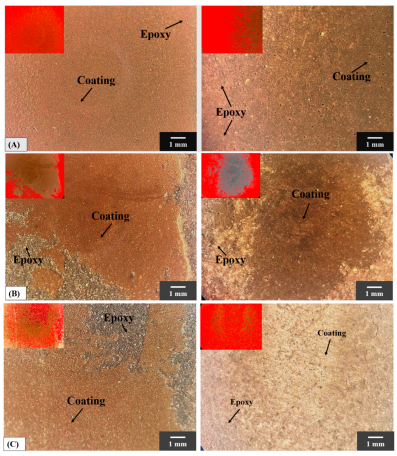


Figure 11 • Representative surfaces from the pull-off adhesion test (ASTM C633). Left: coating surfaces on (**A**) glass, (**B**) steel, and (**C**) aluminum after dolly removal. Right: Corresponding dolly faces imaged showing complementary fracture features and residual coating/epoxy.

These observations confirm that the coatings were well anchored to all substrates, and that the internal cohesion of the aluminosilicate layer is the weakest link governing the ultimate strength. The false-color insets represent attempts to quantify the relative fractional areas of epoxy (red) vs. ceramic film (gray-brown) fracture surface While there is likely no statistical difference between steel and aluminum samples, the glass specimens stand out as having the most epoxy surface revealed. Also the two colors seem to be more evenly dispersed, which means that the failure crack may run closer to the top surface. In this sample, the less tortuous fracture path might be attributed to smaller grain size and higher strength through the bulk of the DAD film.

Quantitative adhesion data for dry/aerosol-deposited films are rarely reported, as most studies rely on tape or scratch tests. Nevertheless, ISO 14916 [35] recognizes pull-off testing as appropriate for aerosol deposition and other spray-applied coatings, and ASTM C633/D4541 [24, 25] provide the standard testing framework. In this context, the adhesion values obtained here (18–25 MPa) fall within the range reported for dense ceramic coatings produced by other physical deposition methods (~20–30 MPa under standard conditions [36, 37]), while cold spray metallic systems subjected to extensive surface pretreatment can achieve values exceeding 50 MPa [37]. Thus, the present results demonstrate that DAD-AS ceramic coatings can exhibit robust and reliable adhesion.

3.5. Scratch adhesion

Scratch testing is another way to measure cohesion strength and adhesion strength between film and substrate. **Figure 12** shows one of nine scratch tests (track 2 of sample A1) made in coatings deposited on aluminum. Cohesive failure corresponds to the critical load (Lc1) where radial cracks first appear along the edge of the track. Adhesive failure corresponds to the second critical load (Lc2) where these cracks coalesce to form bridged regions and the substrate first becomes exposed as a result of coating spallation. There is a clear indication of the onset of interfacial failure and loss of adhesion to the substrate as thereafter the reflective surface of the aluminum is revealed [38]. Values for Lc1 and Lc2 (mean of three scratch tests on each of three samples, A1, A2, A3) are given in **Table 7**.

Figure 13 shows a representative track (one of nine) in coatings on the stainless steel: no Lc1 or Lc2 failures are observed. Eight of nine tracks were clean, continuous, and all but featureless at low magnification. The higher magnification image of the highest load (25 N) end region shows some evidence of minor cracking, but no instances of delamination that bridge the scratch width. The DAD AS coatings on steel therefore display very high adhesion strength. We believe this can be attributed to the robust anchor layer and subsequent high-quality buildup of the film via efficient impact consolidation. Again, we believe that the ultrafine and uniform grain structure provides mechanisms for ductile strain in these ceramic coatings, namely grain boundary sliding and rotation (grain boundary mediated plasticity). The high magnification image in **Figure 12** appears to show a pile-up occurring along the rims of the track (note the slightly lighter shade). Indeed, nano–micro-cracking may be present but not seen at this magnification. Unusual toughness appears to impede crack growth and resist major cohesive failure.

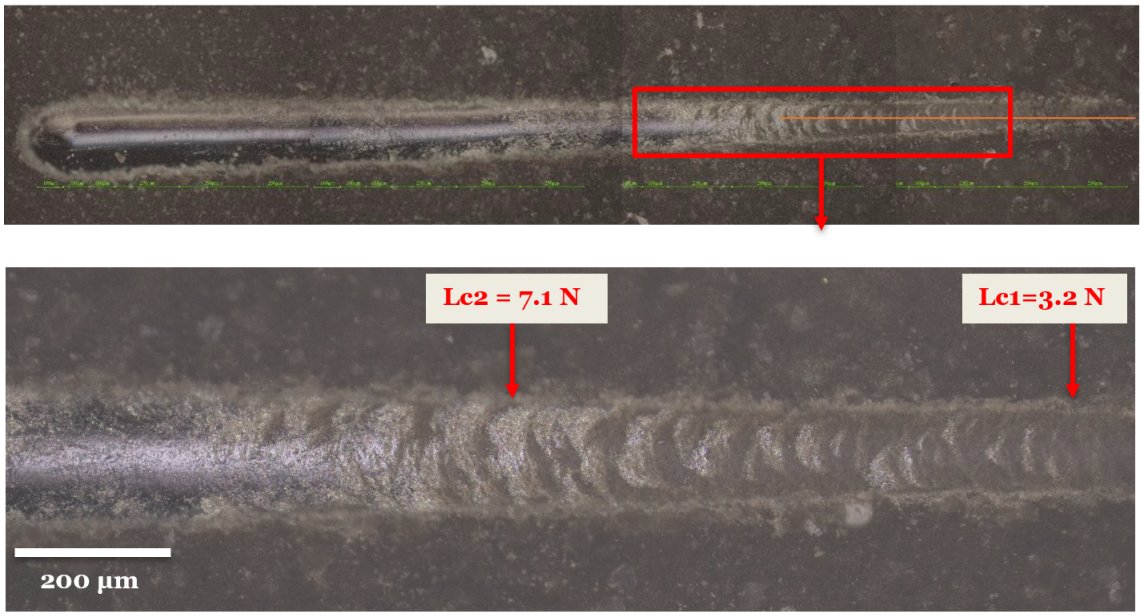


Figure 12 • Example 5 mm long scratch track with magnified view of Lc1 and Lc2 failure zone of DAD AS coating on aluminum.

Table 7 • Mean critical loads (N), Lc1 and Lc2, obtained for three different coatings on aluminum.

Sample number	A1	A2	A3
Lc1 mean (N)	2.53 ± 0.88	5.17 ± 0.82	5.47 ± 0.74
Lc2 mean(N)	6.77 ± 0.54	10.16 ± 1.36	10.14 ± 1.19

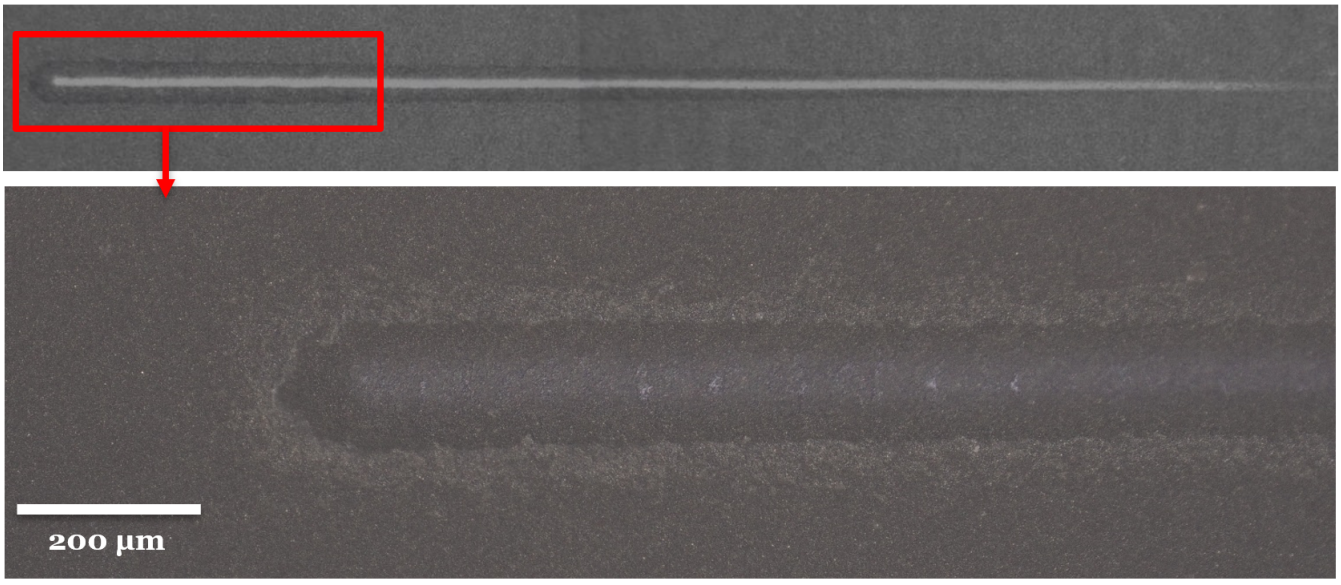


Figure 13 • Example 5 mm long scratch track on steel showing no indications of Lc1 or Lc2 failures, with magnified view at its end.

4. Discussion

The combination of mechanical tests performed revealed interesting behavior for DAD AS films. First and foremost, DAD AS proved to significantly increase the hardness of metallic surfaces. The coating increased the surface hardness of aluminum from H = 1.6 to H = 4.2 GPa. For steel, hardness increased from H = 3.13 GPa to H= 5.93 GPa, which is in good agreement with reported Vickers hardness of some common feldspar/plagioclase volcanic glasses (HV = 5–7 GPa) [39]. Comparison with silicate-based coatings produced by other spray methods gives perspective. Fang et al. [40] deposited Al–SiO_2 composite coatings by cold spray in thicknesses of 200–300 μm, reporting microhardness values (100–200 HV, ≈1–2 GPa) that increase with silica content but remain well below those obtained in the present work. Plasma-sprayed glass–ceramic coatings of [41] an aluminosilicateon stainless steel reached a hardness of 6.8 GPa at coating thicknesses of 150–250 μm. Mishra et al. [42] reported plasma-sprayed fly ash coatings, containing silica, alumina, and mullite phases, with hardness in the range of 800–1000 HV (≈8–10 GPa) at thicknesses of 300–400 μm. Notably, these thermal-sprayed coatings achieve their high hardness at thicknesses that are much greater than those used in the present study. The hardness achieved in steel DAD coatings in the current work (5.93 GPa) seems impressive considering the room temperature DAD process with no melting or sintering.

Elastic moduli obtained from indentation tests were essentially equal on the two metals (E = 48–49 GPa). These modulus values are considerably lower than either of the two bare metals, and lower than a reported value for crystalline albite (117 GPa) and common alkali aluminosilicate glasses (69–86) [43], of which our AS feedstock might be considered a composite. So, in the case of steel, where we believe the best RTIC (room temperature impact consolidation) took place, the AS coatings present simultaneously high hardness and high compliance. Previous DAD work utilizing a complex volcanic mineral mix (lunar simulant) for DAD feedstock showed the same hardness–modulus trends on steel, and also impressive strain to failure for coatings on Kapton [10]. Such mechanical behavior exemplifies the unique benefits of nanocrystalline (NC) and ultrafine-grained (UFG) materials [44]. While we cannot claim Hall–Petch behavior at this point, it is possible that the effect could account for differences across substrates, with hardness increasing from aluminum to glass to steel, and perhaps grain size decreasing in that order. TEM analysis is necessary to accurately determine crystallite size. Differences in remnant nano-porosity and therefore density can also account for the differences, but accurate density measurement of AD films is challenging and remains absent in the literature.

The idea is that harder and stiffer substrates promote more efficient particle fracture and fragmentation during impact, enabling the growth of denser, thicker, more uniform, and smaller particle coatings. This aligns with the broader kinetic impact process literature. Wang et al. [45] demonstrated analogous substrate-dependent hardening in cold-sprayed copper, where harder backings improved particle deformation. Similarly, Schubert et al. [17] attributed enhanced densification in AD ceramics to substrate-mediated energy transfer. The convergence of these trends across disparate deposition methods (cold spray, AD) underscores the universality of substrate–property relationships in kinetic particle spray coating technologies.

Calvo et al. 2022 [10] reported both similar hardness (3.5–3.7 GPA) and modulus (68 GPa) for DAD lunar regolith on glass and steel. In the current work, the lower elastic modulus (E = 38 GPa) for the glass coating compared to steel might be attributed to the modulus of the glass itself, since the thickness on glass was about half that on steel (6 μm vs. 10 μm), and the compression zone below the indent may be approaching the substrate. Images of the indents in **Figure 10** may offer another explanation for the low E values. These particular indents may not be representative as only these few were located post-test due to necessary search times on the SEM. These may, in fact, be “low value” indents that may have probed into a defective, highly cratered or porous region at the surface [46]. Polished depth may not have been adequate to fully reach into the bulk of the film for fear of thickness reduction to the point of violating the 10% penetration depth rule, especially for glass. Thus, the elastic modulus distribution may be skewed to the low side due to incorporation of some of these data. Further nanoindentation studies with measurement at variable film depths are warranted.

The tensile pull and scratch test together indicate high adhesion strength for DAD AS. The superior performance of the films on steel, especially concerning scratch testing, can be attributed to a more effective anchor layer. The shear deformation of the steel with initial impacts (seen in **Figure 6**) is expected to enhance particle intrusion and mechanical interlocking, and therefore interfacial stability. In contrast, aluminum’s lower hardness and modulus reduced fragmentation efficiency, leaving relatively larger and poorly consolidated particles and cracks that hinder uniform deposition and limit coating thickness. These claims are consistent with prior research [32]. The poor anchor layer allowed buckling and spallation of the film from the aluminum at modest scratch loading. The scratch test observations also conform to the model presented by [47], wherein high hardness coatings with H > 5 GPa (i.e., DAD AS) on low hardness substrates (i.e., aluminum) can fail in through-thickness fracture including tensile cracking behind the indenter, conformal cracking as the coating is bent into the scratch track, and Hertzian cracking. Buckling spallation ahead of the crack is common for thin coatings <10 μm, as we see with these films. Hard coatings (i.e., DAD AS) on moderately hard substrates (i.e., steel) undergo interfacial failure, but that threshold was not reached. The clean groove formation with no cracking seen in DAD AS on steel is reminiscent of a soft coating, meaning there is some (super) plasticity exhibited by the ceramic film. The film on aluminum, whose scratch track does accumulate radial cracks, does not exhibit such impressive plasticity, and again we attribute this to a larger crystallite size, larger defects, and perhaps lesser amorphization.

Evidence of plasticity in DAD AS is present in both indent and scratch tests (on steel). The absence of crack extension from the corners of indents (**Figure 10**) suggests strain via crystallite/grain mobility. What appears to be pile-up on both sides of the scratch trench in **Figure 13** without visible radial cracks also suggests grain mobility. This plasticity is afforded to the ceramic coatings by the ultrafine grain structure. We hypothesize that we are witnessing grain boundary-mediated plasticity via grain boundary sliding and grain rotation [44, 47]. In addition to particle comminution, the added amorphization during DAD also enhances these mechanisms, as it is known that as the glassy phase present at grain boundaries increases relative to crystalline core, plasticity increases [47].

5. Conclusions

This work demonstrates the first successful fabrication of robust, nano-scale, mixed crystalline–amorphous aluminosilicate (AS) ceramic thick films via dry aerosol deposition (DAD) using natural igneous mineral crushing fines as feedstock. Compared to the feedstock, XRD confirmed additional impact-driven amorphization in the film. Substrate hardness influenced first and second stage coating morphology, densification, and mechanical performance, with intermediate-hardness, high-modulus stainless steel providing an optimal balance of impact energy dissipation and particle fracture, yielding the hardest and most uniform films. Berkovitch hardness of 5.9 GPa was measured for coatings on steel, compared to 4.2 GPa on aluminum. Tensile pull testing proved robust bonding, with average strengths of 25 MPa for coatings on steel, and 21 MPa on aluminum, with failure mode a mix of film cohesive failure and glue failure rather than adhesive (substrate–coating interface) failure. Scratch testing also revealed superior biaxial shear strength for coatings on steel, with clean tracks showing virtually no evidence of buckling or cracking up to the maximum vertical load (25 N). On the other hand, coatings on aluminum failed both cohesively and adhesively, at average loads of 4.39 N and 9.0 N respectively, evidenced by radial cracking, crack bridging across the track, and localized spallation.

Together, these results indicate that the higher hardness and stiffness of the steel substrate promotes the aerosol deposition of higher quality coatings, perhaps with higher density and/or reduced particle size by more efficient particle fragmentation, chemical bonding, and mechanical keying. The absence of cracks at indentations and radial cracks along the scratch track suggests ductility in the DAD ceramic films. The ultrafine grain structure and accompanying high amorphous grain boundary volume is believed to give grain boundary-mediated plasticity, providing the unique combination of enhanced surface hardness and increased compliance to metallic surfaces, especially steel. Overall, this study suggests that natural aluminosilicate may be a promising, cost-effective, and environmentally friendly feedstock for DAD ceramic coatings. The demonstrated substrate-dependent coating deposition and performance behavior gives guidance for designing DAD-coated surfaces with resistance to mechanical, chemical, and corrosion damage, and perhaps interesting tribology properties.

Acknowledgments

The authors gratefully acknowledge Katie Ringler and John Curry of Sandia National Labs for scratch testing and analysis.

Funding

This research was sponsored, in part, by the United States Army Research Lab under grant #W911NF2020190.

Author contributions

Conceptualization, A.K. and P.F.; methodology, A.K. and P.F.; formal analysis, A.K. and P.F.; investigation, A.K.; resources, P.F.; data curation, A.K.; writing-original draft preparation, A.K.; writing-review and editing, P.F.; supervision, P.F.; funding acquisition, P.F. All authors have read and agreed to the published version of the manuscript.

Conflict of interest

The authors declare that they have no competing interests. The sponsors played no role in the conception, execution, interpretation, or writing of this manuscript.

Data availability statement

The data supporting the findings of this publication can be made available upon request.

Additional information

Received: 6 October 2025

Accepted: 17 February 2026

Published: 3 March 2026

Academia Nano: Science, Materials, Technology papers should be cited as *Academia Nano: Science, Materials, Technology 2026*, ISSN 3065-9736, https://doi.org/10.20935/AcadNano8182. The journal's official abbreviation is *Acad. Nano: Sci. Mat. Tech.*

Publisher's note

Academia.edu Journals stays neutral with regard to jurisdictional claims in published maps and institutional affiliations. All claims expressed in this article are solely those of the authors and do not necessarily represent those of their affiliated organizations, or those of the publisher, the editors and the reviewers. Any product that may be evaluated in this article, or claim that may be made by its manufacturer, is not guaranteed or endorsed by the publisher.

Copyright

© 2026 copyright by the authors. This article is an open access article distributed under the terms and conditions of the Creative Commons Attribution (CC BY) license (https://creativecommons.org/licenses/by/4.0/).

References

1. Akedo J. Aerosol deposition of ceramic thick films at room temperature: densification mechanism of ceramic layers. J Am Ceram Soc. 2006;89(6):1834–9. doi: 10.1111/j.1551-2916.2006.01030.x

2. Choi S, Lim J-H, Kang E-Y, Kim H, Kong Y-M, Jeong D-Y. Deposition behavior of glass thick film formation on substrates with different hardness by aerosol deposition. J Asian Ceram Soc. 2021;9(3):1128–36. doi: 10.1080/21870764.2021.1943155

3. Lee D-W, Kim H-J, Kim Y-N, Jeon M-S, Nam S-M. Substrate hardness dependency on properties of Al_2O_3 thick films grown by aerosol deposition. Surf Coat Technol. 2012;209:160–8. doi: 10.1016/j.surfcoat.2012.08.012

4. Fuierer P, Calvo R, Strobel G. Dense, nano-grained, multiphase ceramic coatings by dry aerosol deposition of lunar regolith simulant. Addit Manufact. 2020;35:101304. doi: 10.1016/j.addma.2020.101304

5. Kim H-K, Lee S-H, Lee S-G, Lee Y-H. Densification mechanism of BaTiO3 films on Cu substrates fabricated by aerosol deposition. Electron Mater Lett. 2015;11(3):388–97. doi: 10.1007/s13391-015-4419-0

6. Exner J, Linz M, Kita J, Moos R. Making powder aerosol deposition accessible for small amounts: A novel and modular approach to produce dense ceramic films. Int J Appl Ceram Technol. 2021;18(6):2178–96. doi: 10.1111/ijac.13841

7. Lee DW, Kim HJ, Kim YH, Yun YH, Nam SM. Growth process of α-Al_2O_3 ceramic films on metal substrates fabricated at room temperature by aerosol deposition. J Am Ceram Soc. 2011;94(9):3131–8. doi: 10.1111/j.1551-2916.2011.04493.x

8. Valdez A, Fuierer P. Dry aerosol deposition of barium neodymium titanate microwave dielectric. Int J Appl Ceram Technol. 2025;22(6):e70039. doi: 10.1111/ijac.70039

9. Hanft D, Exner J, Schubert M, Stocker T, Fuierer P, Moos R. An overview of the aerosol deposition method process: process fundamentals and new trends in materials applications. J Ceram Sci Tech. 2015;6(3):147–82. doi: 10.4416/JCST2015-00018

10. Calvo R, Fuierer P. Mechanical integrity of ceramic coatings on Kapton made by a dry aerosol deposition of lunar mare simulant. Int J Appl Ceram Technol. 2022;20(1):395–409. doi: 10.1111/ijac.14235

11. Naoe K, Nishiki M, Yumoto A. Relationship between impact velocity of Al2O3 particles and deposition efficiency in aerosol deposition method. J Therm Spray Technol. 2013;22(8):1267–74. doi: 10.1007/s11666-013-0031-8

12. Lee BK, Jung J-H, Hahn BD, Yoon WH, Park D-S, Choi JJ, et al. Dense Yttria Film Deposited on a Plasma-Sprayed Al_2O_3 Coating by Aerosol Deposition. J Ceram Sci Technol. 2011;2(4):197–202. doi: 10.4416/JCST2011-00026

13. Gaida NA, Nishiyama N, Masuno A, Holzheid A, Ohfuji H, Schürmann U, et al. Synthesis of Al2O3/SiO2 nano-nano composite ceramics under high pressure and its inverse Hall–Petch behavior. J Am Ceram Soc. 2016;100(1):323–32. doi: 10.1111/jace.14551

14. Shibuya T, Mizuno T, Iuchi A, Hasegawa M. Formation of mullite coating by aerosol deposition and microstructural change after heat exposure. Mater Trans. 2020;61(3):540–7. doi: 10.2320/matertrans.MT-M2019354

15. Steinmann PA, Hintermann HE. A review of the mechanical tests for assessment of thin-film adhesion. J Vacuum Sci Technol a Vacuum Surf Films. 1989;7(3):2267–72. doi: 10.1116/1.575926

16. Miyakawa T, Matsuzawa R, Katayama M, Takegawa N. Reconsidering adhesion and bounce of submicron particles upon high-velocity impact. Aerosol Sci Technol. 2013;47(5):472–81. doi: 10.1080/02786826.2013.763895

17. Schubert M, Hahn M, Exner J, Kita J, Moos R. Effect of substrate hardness and surface roughness on the film formation of aerosol-deposited ceramic films. Funct Mater Lett. 2017;10(4):1750045. doi: 10.1142/S179360471750045X

18. Daneshian B, Gaertner F, Assadi H, Hoeche D, Weber W, Klassen T. Size effects of brittle particles in aerosol deposition—molecular dynamics simulation. J Therm Spray Technol. 2021;30(3):503–22. doi: 10.1007/s11666-020-01149-9

19. Borrego R, Mercado D, Fuierer P. Increased bend strength of glass by dry aerosol deposition of alumina. Ceram Int. 2025;51(18):25819–27. doi: 10.1016/j.ceramint.2025.03.266

20. Saunders R, Johnson SD, Schwer D, Patterson EA, Ryou H, Gorzkowski EP. A self-consistent scheme for understanding particle impact and adhesion in the aerosol deposition process. J Therm Spray Technol. 2021;30(3):523–41. doi: 10.1007/s11666-021-01164-4

21. ISO 14577-1:2015. Metallic Materials—Instrumented Indentation Test for Hardness and Materials Parameters. Geneva: International Organization for Standardization; 2015.

22. Adamczyk J, Fuierer P. Compressive stress in nano-crystalline titanium dioxide films by aerosol deposition. Surf Coat Technol. 2018;350:542–9. doi: 10.1016/j.surfcoat.2018.07.015

23. ASTM E2546-15. Standard Practice for Instrumented Indentation Testing. West Conshohocken (PA): ASTM International; 2015.

24. ASTM C633-13(2021). Standard Test Method for Adhesion or Cohesion Strength of Thermal Spray Coatings. West Conshohocken (PA): ASTM International; 2021.

25. ASTM D4541-22. Standard Test Method for Pull-Off Strength of Coatings Using Portable Adhesion Testers. West Conshohocken (PA): ASTM International; 2022.

26. ASTM C1624-05(2015). Standard Test Method for Adhesion Strength and Mechanical Failure Modes of Ceramic Coatings by Quantitative Single Point Scratch Testing. West Conshohocken (PA): ASTM International; 2015.

27. ASTM D3359-23. Standard Test Methods for Rating Adhesion by Tape Test. West Conshohocken (PA): ASTM International; 2023.

28. Nohava J. How to deal with roughness in nanoindentation measurements [Application Report]. Graz: Anton Paar GmbH; 2022 [accessed on 16 February 2026]. Available from: https://www.anton-paar.com/se-en/services-support/webinars/detail/event/how-to-deal-with-roughness-in-nanoindentation-measurements/?utm_source=chatgpt.com

29. Assadi H, Gärtner F, Stoltenhoff T, Kreye H. Bonding mechanism in cold gas spraying. Acta Mater. 2003;51(15):4379–94. doi: 10.1016/S1359-6454(03)00274-X

30. Exner J, Schubert M, Hanft D, Kita J, Moos R. How to treat powders for the room temperature aerosol deposition method to avoid porous, low strength ceramic films. J Eur Ceram Soc. 2019;39(2–3):592–600. doi: 10.1016/j.jeurceramsoc.2018.08.008

31. Wu Y, Choy K-L. The microstructure of alumina coatings prepared by aerosol assisted spray deposition. Surf Coat Technol. 2004;180–1:436–40. doi: 10.1016/j.surfcoat.2003.10.078

32. Khansur NH, Eckstein U, Li Y, Hall DA, Kaschta J, Webber KG. Revealing the effects of aerosol deposition on the substrate-film interface using NaCl coating. J Am Ceram Soc. 2019;102(10):5763–71. doi: 10.1111/jace.16489

33. Akedo J. Room Temperature Impact Consolidation (RTIC) of fine ceramic powder by aerosol deposition method and applications to microdevices. J Therm Spray Technol. 2008;17(2):181–98. doi: 10.1007/s11666-008-9163-7

34. Xiong Y, Kang K, Bae G, Yoon S, Lee C. Dynamic amorphization and recrystallization of metals in knietic spray process. Appl Phys Lett. 2008;92:194101. doi: 10.1063/1.2928218

35. ISO 14916:2017. Thermal Spraying—Determination of Tensile Adhesive Strength. Geneva: International Organization for Standardization; 2017.

36. Choudhuri A, Mohanty PS, Karthikeyan J. Bioceramic composite coatings by cold spray technology. Proceedings of the 2009 International Thermal Spray Conference; 4–7 May 2009; Las Vegas, NV, USA. 2009. doi: 10.31399/asm.cp.itsc2009p0391

37. Prashar G, Vasudev H. A comprehensive review on the analysis of adhesion strength of cold spray deposits. Result Surf Interfaces. 2024;16:100263. doi: 10.1016/j.rsurfi.2024.100263

38. Bull SJ, Berasetegui EG. An overview of the potential of quantitative coating adhesion measurement by scratch testing. Tribol Int. 2006;39(2):99–114. doi: 10.1016/j.triboint.2005.04.013

39. Webster RI, Bansal NP, Salem JA, Opila EJ, Wiesner VL. Characterization of thermochemical and thermomechanical properties of eyjafjallajökull volcanic ash glass. Coatings. 2020;10(2):100. doi: 10.3390/coatings10020100

40. Fang L, Xu Y, Gao L, Suo X, Gong J, Li H, et al. Cold-sprayed aluminum-silica composite coatings enhance antiwear/anticorrosion performances of AZ31 magnesium alloy. Adv Mater Sci Eng. 2018;2018(1):3215340. doi: 10.1155/2018/3215340

41. Faeghinia A, Shahgoli N, Jabbari E. Phlogopite glass-ceramic coatings on stainless steel substrate by plasma spray. Adv Ceram Progress. 2016;2:16–21. doi: 10.30501/acp.2016.70019

42. Mishra SC, Satpathy A, Singh KP, Sethy S, Padmanabham PVA, Sreekumar KP, et al. Plasma spray coating of fly ash on metals for tribological application. Proceedings of the International Seminar on Mineral Processing Technology; 8–10 March 2006; Chennai, India. 2006.

43. Yin D, Montazerian M, Hunziker P, Cornejo IA, Mauro JC. Perspective on glass properties influencing perlite expansion and strength. J Am Ceram Soc. 2025;108(10):e70055. doi: 10.1111/jace.70055

44. Kim HS, Bush M. The effects of grain size and porosity on the elastic modulus of nano-crystalline materials. Nanostruct Mater. 1999;11(2):361–7. doi: 10.1016/S0965-9773(99)00052-5

45. Wang H, Li P, Guo W, Ma G, Wang H. Copper-based composite coatings by solid-state cold spray deposition: a review. Coatings. 2023;13(3):479. doi: 10.3390/coatings13030479

46. Jang B-K, Matsubara H. Influence of porosity on hardness and Young's modulus of nanoporous EB-PVD TBCs by nanoindentation. Mater Lett. 2005;59(27):3462–6. doi: 10.1016/j.matlet.2005.06.014

47. Meyers MA, Mishra A, Benson DJ. Mechanical properties of nanocrystalline materials. Prog Mater Sci. 2006;51(4):427–556. doi: 10.1016/j.pmatsci.2005.08.003